Optimizing Tissue Clearing Methods for Improved Imaging of Whole-Mount Retinas

Aubin Mutschler,[1,2,3] Volha V. Malechka,[1,2] Petr Baranov,[1,2] Jonathan R. Soucy[1,2,*]

1. The Schepens Eye Research Institute of Massachusetts Eye and Ear, Boston, MA 02114
2. Department of Ophthalmology, Harvard Medical School, Boston, MA 02114
3. Department of Neuroscience, Middlebury College, Middlebury, VT 05753

*corresponding author: jonathan_soucy@meei.harvard.edu

Abstract

Gene and cell therapies are promising approaches for restoring vision in developmental and advanced optic neuropathies. However, these therapeutic approaches must be accurately evaluated through a combination of approaches, including advanced imaging, to reach the clinic. We present a whole-mount tissue-clearing methodology to improve imaging of donor neuron integration in the retina following transplantation in mice. Mouse retinas were processed using five different clearing methods, comparing tissue transparency, pigmentation, and immunohistochemical clarity. Among the tested methods, ScaleS consistently outperformed its peers, demonstrating a 46% increase in tissue transparency and an 89% increase in immunohistochemical clarity compared to control. We developed a modified version of ScaleS, termed ScaleH, by adding polyvinyl alcohol to reduce fluorescence decay and enhance sample stability. ScaleH maintained fluorescence stability over extended periods (32% less decay) and proved compatible with immunolabeling and endogenous fluorescent reporters, enabling improved visualization of transplanted human stem cell-derived retinal neurons in the mouse retina. Moreover, ScaleH also improved optic nerve imaging, demonstrating the potential for broader neurobiological applications. Our clearing workflow supports robust, high-resolution imaging for evaluating the integration of transplanted cells in regenerative studies.

Introduction

As the global population ages, eye diseases such as glaucoma, age-related macular degeneration, and diabetic retinopathy are becoming increasingly prevalent, underscoring an urgent need for therapeutic advancements (Hashemi et al., 2017). Gene therapies and stem cell transplantation are promising approaches to restore vision (Nanegrungsunk et al., 2022). The eye is particularly well-suited for these therapies due to its accessibility, immune privilege, and localized effects afforded by the blood-ocular barriers (Ghoraba et al., 2022). However, the

precise targeting of therapies needs to be monitored closely. For example, retinal ganglion cell (RGC) transplantation requires integration into the ganglion cell layer and axon extension through the optic nerve to restore vision (Zhang et al., 2021)(Soucy et al., 2023a). These challenges underscore the importance of robust models and advanced imaging techniques to refine and evaluate therapeutic approaches.

Understanding the molecular and cellular mechanisms underlying retinal function is essential for advancing our understanding of ocular development and disease. Moreover, given its accessibility as a part of the central nervous system, the retina offers a unique model for studying neurological processes beyond vision, with implications for broader biomedical applications (London et al., 2013).

Imaging is a vital tool for elucidating the interactions between novel treatments, molecular mechanisms, and the structural complexity of the retina. Optical coherence tomography (OCT) is the gold standard for non-invasive, three-dimensional imaging of the in-vivo eye in humans and animals, yet it lacks the resolution needed to resolve the detailed cellular and molecular makeup of the retina (Huang et al., 1991)(Jagodzinska et al., 2017). High-resolution approaches, such as single-photon confocal microscopy, allow visualization of fine structures in thin tissue samples, whereas two-photon microscopy offers greater depth penetration but is limited by photobleaching and signal-to-noise challenges (Cheng et al., 2023). Alternatively, light-sheet fluorescence microscopy enables rapid, detailed three-dimensional imaging but often lacks the precision required for smaller structures, making confocal microscopy the preferred choice for retinal studies (Prahst et al., 2020).

Despite advances in imaging technology, optical limitations persist due to inherent tissue properties. Light scattering caused by structural heterogeneity and refractive index mismatches between lipid membranes and aqueous interfaces contributes to tissue opacity, limiting imaging depth and resolution, especially in thicker tissue samples (Richardson & Lichtman, 2015) (Chung et al., 2013). To overcome these obstacles, tissue-clearing techniques have been developed to reduce opacity (Richardson & Lichtman, 2015). Active clearing involves external forces to remove lipids, requiring harsh reagents and involved protocols, while passive clearing uses chemical diffusion through aqueous or organic solvents (Chung et al., 2013). Hydrophilic-based solvents are preferred for fluorescent imaging due to their ability to preserve fluorescence and minimize tissue shrinkage (Renier et al., 2014). Recently, ultrafast clearing protocols have been developed to reduce processing times and streamline experimental workflows (Tomer et al., 2014)(Matsumoto et al., 2019). In facilitating high-resolution imaging, it is well suited for cellular visualizations of the retina.

In this study, we compare five ultrafast tissue clearing protocols—ScaleS (Hama et al., 2015), FOCM (X. Zhu et al., 2019), OptiMuS (K. Kim et al., 2022), MACS (J. Zhu et al., 2020), and Visikol

HISTO-1 (Villani et al., 2013)—to identify an optimal method for retinal applications. Our evaluation focused on three critical factors: tissue transparency, compatibility with immunostaining markers, and fluorescence retention. ScaleS emerged as the optimal solution, and we developed a protocol tailored for retinal applications. To extend its utility, we modified the ScaleS recipe to include a self-hardening mechanism that preserves fluorescence over prolonged periods. Using this optimized protocol, we demonstrated the compatibility with stem cell-derived RGC transplantation in the retina and extended its application to the optic nerve, illustrating its versatility for other neural tissues beyond the retina.

Methods and Materials

Donor Cell Transplantation. All animal procedures were approved by the Institutional Animal Care and Use Committee (IACUC) at the Schepens Eye Research Institute. Donor RGC transplantations were performed as previously described (Soucy et al., 2023b).

Donor retinal ganglion cells (RGCs) were differentiated from H9-BRN3B:tdTomatoThy1.2-hESCs using a 2D differentiation protocol (Sluch et al., 2017). Thy1.2-positive RGCs were isolated via magnetic microbead sorting, as previously described [cite]. For transplantation, 20,000 RGCs suspended in 1 µL of N2B27 medium [1x GlutaMAX, 1x antibiotic antimycotic, 1% N2 supplement, and 2% B27 supplement in 50:50 1x DMEM/F12:Neurobasal medium] were injected intravitreally into the eyes of adult mice (C57BL/6-background, 4–8 months old, both sexes) under general anesthesia (intraperitoneal injection of ketamine/xylazine) and local anesthesia (0.5% proparacaine eye drops). Injections were performed using a beveled glass microneedle (80 µm inner diameter) at a flow rate of 1 µL/min. Animals were maintained on a 12-hour light/dark cycle and euthanized 3 days post-transplantation via CO2 inhalation.

Mouse retina sample preparation. Retinal tissue and optic nerve samples were collected from wild-type (C57BL/6-background) mice aged 1-2 years of both sexes. Mice were euthanized by CO2 asphyxiation.

Following euthanasia, the eyes were enucleated, and the cornea was punctured (for whole mounts only) to improve the diffusion of the fixative. Samples were fixed in 4% paraformaldehyde (PFA; w/v in phosphate-buffered saline (PBS)) overnight on a shaker at 4C. PFA was prepared as frozen aliquots and thawed immediately before use. Eyes were washed with 0.01M PBS after fixation. For retinal whole mounts, retinas were then collected, and

relaxing incisions were placed at equal distances around the retina for flat mounting. Isolated retinas were stored in 0.01M PBS overnight at 4°C for future use.

For retinal sections, whole eyes were sent to the Schepens Eye Research Institute Morphology Core for paraffin embedding (6 µm sections). To stain paraffin-embedded sections, sections were first deparaffinized in xylene substitute I, washed with serial dilutions of ethanol, and then demasked for 30 min using sodium citrate buffer (10 mM Sodium citrate, 0.05% tween20, pH 6.0). To investigate an endogenous fluorophore signal, retinas from Cx3cr1-GFP mice were dissected, permeabilized, blocked, stained, cleared, and imaged within 12 hours.

Clearing solutions preparation. OptiMuS, FOCM, ScaleSQ(5), and ScaleS4 were prepared as previously described (Kim et al., 2022) (Zhu et al., 2019) (Hama et al., 2015). In brief, to prepare the OptiMuS solution, 100 mM Tris (Sigma-Aldrich) and 0.34mM EDTA (Invitrogen) were dissolved in ddH_2O and titrated to a pH of 7.5 using 1N HCl, while being stirred continuously (200 rpm). After the buffer was prepared, 75% (w/v) Histodenz (Sigma-Aldrich) was added and dissolved at 60°C with continuous stirring (200 rpm). Subsequently, 10% (w/v) D-sorbitol (Sigma-Aldrich) and 4M urea (Sigma-Aldrich) were dissolved into the solution under the same conditions (60°C, 200 rpm). The completed OptiMuS solution was cooled to room temperature and stored at 4°C for later use.

To prepare the FOCM solution, 30% (w/v) urea and 20% (w/v) d-sorbitol were dissolved in DMSO with continuous stirring (200 rpm) overnight at room temperature. After complete dissolution, glycerol (Sigma-Aldrich) was added to the solution while stirring continued. The FOCM solution was stored at room temperature for later use.

To prepare the ScaleSQ(5) solution, 22.5% (w/v) D-(–)-sorbitol and 9.1M urea were dissolved in ddH_2O with continuous stirring (200 rpm). Subsequently, 5% (w/v) Triton X-100 was added and stirred until fully dissolved. The solution was titrated to a pH of 8.2. The complete ScaleSQ(5) solution was stored at room temperature for future use.

To prepare ScaleS4, 40% (w/v) D-(–)-sorbitol, 10% (w/v) glycerol, 4M urea, and 20% (v/v) dimethyl sulfoxide (FisherSci) were dissolved in ddH_2O and titrated to a pH of 7.8. Subsequently, 0.2% (w/v) Triton X-100 was added, and the solution was stored at room temperature for future use.

Lastly, to prepare our custom ScaleH combination clearing and mounting solution, two solutions (A and B) were combined at 55°C. Solution A was prepared by dissolving 15% (w/v) polyvinyl alcohol and 15% (w/v) glycerol in deionized water, followed by overnight incubation at room temperature with rocking. The solution was subsequently heated at 55°C until clear. Solution B was prepared by dissolving 3 M urea, 22.5% (w/v) D-(–)-sorbitol, 0.1 M Tris-HCl, 2.5% (w/v) 1,4-

Diazabicyclo[2.2.2]octane (DABCO), and 15% (v/v) DMSO in deionized water at 55°C with continuous stirring. Once both solutions were warm and fully dissolved, Solution A was added to Solution B with stirring until homogenized. The pH was adjusted to 8.7 using HCl or NaOH. The final ScaleH solution was aliquoted into vials and stored at –20°C for future use.

Immunohistochemistry. For immunofluorescent staining of whole-mount retinas and retinal sections, tissue was permeabilized with the OptiMuS (20% (w/v) DMSO and 2% (w/v) Triton X-100 in 0.01M PBS), FOCM (30% (w/v) sucrose in 0.01M PBS), ScaleS (20% (w/v) sucrose in 0.01M PBS), Militenyi Biotec™ MACS®, or Visikol® HISTO™ permeabilization solutions for each corresponding clearing solution as previously described or according the manufacturer's protocol.

Samples were incubated in the FOCM and ScaleS permeabilization solutions for 4 hours at 4°C or the OptiMuS permeabilization solution for 4 hours at 37°C and subsequently washed three times with 0.1% triton X-100 and 0.1% tween-20 in 0.01M PBS (PBST) in 10-minute intervals. Permeabilization and wash steps for MACS and Visikol HISTO™ were completed following the Militenyi Biotec™ mouse brain hemispheres and Visikol® protocols. Control samples were washed three times with PBST in 10-minute intervals.

Retinas were then blocked against non-specific antibody binding using the OptiMuS blocking buffer (10% (w/v) bovine serum albumin in 0.01M PBS), the Visikol® HISTO™ blocking solution, or our custom blocking buffer (10% goat serum, 1% bovine serum albumin, 0.1% sodium citrate, 0.25% tween-20, 0.25% triton-X, and 0.3M glycine in 0.01 M PBS) as previously described (Soucy et al., 2023b). Samples were incubated for 2 hours at room temperature.

Following blocking, tissue was incubated with primary antibodies in each clearing solution's corresponding staining buffer. For OptiMuS, FOCM, ScaleS, and our control, the staining buffer consists of 1% bovine serum albumin, 0.25% tween-20, and 0.25% triton-X in 0.01M PBS. Staining buffers for MACS® and HISTO™ were prepared according to the manufacturer. A complete list of primary antibodies and their concentrations used in this study is available in **Table S1**. All retinal whole-mounts were incubated with primary antibodies for 60 hours at 4°C. Retinal sections were incubated overnight at 4°C. Samples were washed three times in 1-hour intervals using PBST or the manufacturer's specified wash buffer. After removing any unbound primary antibody, goat anti-chicken (Jackson Immuno), anti-guinea pig (Jackson Immuno), anti-rabbit (Jackson Immuno), and anti-mouse (Jackson Immuno) secondary antibodies were prepared at 1:500 in each staining buffer and incubated for 24 hours at 4°C. Samples were then washed with wash buffer in triplicate to remove any unbound secondary antibody and then incubated with 1 µg/mL DAPI (4',6-diamidino-2-phenylindole) in PBS for 1 hour for whole

mounts and 20 min for sections to stain the cell nuclei. For the MACS and Visikol tissue clearing, samples were dehydrated according to each manufacturer's protocols.

Imaging. Prior to clearing, retinal tissues were visualized using a stereomicroscope to verify flat-mount placement on single concave microscope slides. Initial imaging was done with samples positioned over a white background, illuminated uniformly by an LED ring light (Unitron). Images were captured using a 4K Digital Wi-Fi Microscope (Jiusion-4KScope) positioned within the ring light. To qualitatively assess sample transparency, selected samples were imaged and placed above the Harvard Medical School logo.

Transparency images were taken using an Olympus XM10 microscope with Olympus cellSens Dimension software. Imaging conditions were standardized, including consistent ambient lighting, LED brightness set at 0, exposure time of 174.7 ms, and gain of 8 dB. Images were captured at 2x magnification (1376 × 1038 pixels). For transparency assessment, samples were imaged alongside a Fine Science Tools ruler to ensure complete specimen visualization and clearly delineated demarcation lines.

Samples were prepared for clearing by drying them using an absorption spear and applying 60µL clearing solution onto the microscope slides. The standard clearing protocol utilized a 10-minute incubation, with ScaleS clearing requiring an additional 10-minute ScaleS4 solution incubation post-ScaleSQ treatment. Post-clearing transparency imaging replicated pre-clearing conditions, including ruler superimposition and standardized background illumination. Samples previously imaged with institutional logos were imaged identically post-clearing.

Subsequently, samples were positioned coverslip-down for imaging with a FLUOVIEW FV3000 confocal microscope. Flat retinal regions were selected for imaging using one-way 1024 × 1024 Galvano scanning with frame intervals and step sizes set to 2 µm. Preliminary visualization at 2x magnification was used to determine precise areas of interest, which were subsequently imaged at 20x magnification. Following imaging, samples were stored at room temperature under minimal light exposure to preserve integrity.

Image Analysis. Images were loaded into ImageJ and resliced from the left-hand side, with output rotations applied for consistent orientation. Intensity profile plots for each slice were generated, and data was exported as text files. Results were cleared for subsequent slices.

A custom MATLAB script was then used to analyze the previously generated cell nuclei intensity profile plots. Data files containing slice information were batch-imported and processed using the MATLAB trapz function to calculate the integral of intensity curves for each image slice. Integrals were normalized by dividing by the number of data points along the x-axis. The first

local maximum for each slice was measured, and the largest first local maximum across all slices in a retina was selected to normalize the integrals. Normalized integrals were averaged for each retina.

Microglial analyses focused on flat retinal sections, excluding unsuitable images. Images underwent background subtraction in ImageJ, followed by left-hand side reslicing and 90-degree rotation. A maximum-intensity z-projection was applied, and intensity profiles were generated for analysis. Coordinates corresponding to peak microglial intensities were identified and normalized to a value of 1. Slopes between two peak intensity points were calculated for each clearing solution, with average x and y coordinates recorded for comparative plotting.

Statistical Analysis. Statistical significance was calculated using GraphPad Prism 10, employing an ordinary one-way ANOVA. Data are presented as mean ± standard deviation (*$P < 0.05$, **$P < 0.01$, ***$P < 0.001$, and ****$P < 0.0001$). Each data point within the bar plots represents one flat-mount retina.

Figure Generation. Figures were generated using Adobe Illustrator 2024, Adobe Photoshop 2024, BioRender, and GraphPad Prism 10.

Data/Code Availability. A custom MATLAB script used to measure normalized DAPI intensity (Fig. 3C) is available upon request.

Results

Clearing Improves Transparency of the Retina

To identify the most effective tissue-clearing method for retinal tissue, we evaluated five established clearing solutions based on immunohistochemical compatibility, ease of use, and demonstrated clearing efficacy: ScaleS (Hama et al., 2015), FOCM (X. Zhu et al., 2019), OptiMuS (K. Kim et al., 2022), MACS (J. Zhu et al., 2020), and Visikol HISTO-1 (Villani et al., 2013) . Each solution was applied to mouse retinas, and transparency was assessed.

In preliminary assessments, all solutions except Visikol HISTO-1 qualitatively increased retinal transparency (Fig. 1A). Post-clearing, tissues treated with MACS and Visikol became notably denser and more brittle. Transparency improvements were quantitatively assessed by measuring percentage changes in pixel gray values along defined reference lines (Fig. 1B; SI

Appendix, Fig S1). All clearing agents significantly enhanced transparency compared to PBS controls. FOCM, ScaleS, and MACS, increased transparency by 44%, 46%, and 50% compared to the control, with ScaleS showing the most consistent transparency improvements.

In addition to transparency, we also evaluated pigmentation removal. Tissue pigmentation can cause severe light absorbance and reduce image quality (Zhu et al., 2021). To quantify pigmentation removal, we developed a novel analysis method using a color space map (Zhu et al., 2019)(Hasabeldaim et al., 2023). Using chromaticity diagrams to map color perception, we converted RGB data to the XYZ color space to measure hue differences resulting from each clearing solution (Fig. 1C; SI Appendix, Fig. S2). The distance between each solution's chromaticity value and a true white reference point was calculated to approximate pigmentation clearance (Fig. 1D).

Although differences in chromaticity distances were not statistically significant, ScaleS achieved the shortest distance to true white, achieving a color value 26% closer to true white value than the closest competitor. Furthermore, it displayed minimal variation compared to other solutions, underscoring its consistent performance. Notably, the top-performing reagent in the transparency analysis, ScaleS, also ranked highest in the color-based analysis. Together, these findings identified ScaleS, OptiMuS, MACS, and FOCM as promising solutions for enhancing retinal transparency.

Clearing is Compatible with Retinal Immunostaining

To evaluate the compatibility of the selected clearing solutions with immunostaining, we stained whole retinal flat mounts for key retinal neuron populations. Specifically, photoreceptors, bipolar cells, and retinal ganglion cells were labeled using recoverin, PKC-α, and Brn3a, respectively (Hoon et al., 2014). Samples were counterstained with DAPI to visualize the cell nuclei.

Computationally reconstructed sections of cleared retinal flat mounts showed clear visualization of all cell layers and nuclei in all experimental conditions (Fig. 2A). En-face imaging confirmed specific staining of photoreceptor outer segments, bipolar cells, and retinal ganglion cells for each reagent (Fig. 2B).

Next, we evaluated the preservation of synaptic markers, which is crucial for examining neural connectivity and identifying synaptic pathology in retinal disorders (Graham & Duan, 2020). Immunostaining of retinal sections with synaptic markers VGLUT1 and PSD-95 resulted in correctly localized staining patterns across each clearing method tested (Fig. 2C).

Finally, we examined compatibility with endogenous fluorescent reporter expression using microglia-specific Cx3cr1-GFP reporter mice. Microglia are essential for immune surveillance,

synaptic pruning, and neuroinflammation in the retina (Ramirez et al., 2017). Immunostaining with the microglial marker Iba1 confirmed robust labeling across all clearing protocols. Importantly, clearing procedures did not disrupt endogenous GFP fluorescence in microglia (Fig. 2D).

Tissue Clearing Enhances Full-thickness Immunostaining of the Retina

After establishing immunostaining compatibility, we quantified the clearing effectiveness of each solution by comparing fluorescence intensity across retinal layers. DAPI staining, which labels the nuclei of cells in three distinct retinal layers, served as a benchmark for inter-layer comparison (Fig. 3A). The RGC layer, positioned superficially, was used as a reference for normalization. Bipolar and photoreceptor cell layers, located progressively deeper within the retina, were analyzed to assess tissue transparency.

To quantify DAPI fluorescence penetration, we employed a semi-automated analysis of intensity profiles (Fig. 3B). Integrated fluorescence intensity across retinal layers was calculated and normalized relative to the brightest signal in the RGC layer of each retina. Statistical analyses of normalized intensities revealed that ScaleS (0.98) produced significantly higher nuclear-staining intensities in the retina. Signal intensity was used as a proxy for clearing efficacy, especially within the deepest layer, as the nuclear signal from the photoreceptor layer would be attenuated deeper into the tissue. In contrast to the other clearing solutions tested, FOCM (0.48) and MACS (0.36) produced lower fluorescence intensities, indicating less effective tissue clearing. The reduced signal suggests limited light penetration and decreased visibility of deeper retinal layers, indicating lesser transparency than ScaleS (Fig. 3C).

In addition to nuclear staining, we assessed fluorescence penetration through microglial labeling. Retinal microglia are arranged in two distinct layers, allowing us to evaluate signal attenuation between superficial and deeper layers using slope analysis (Fig. 3D). Peak intensity values from fluorescence profiles were selected to calculate slopes, with a slope closest to zero representing no fluorescence attenuation throughout the retina (Fig. 3E). Through this analysis, we showed the average slopes of ScaleS (m=-0.68) and OptiMuS (m=-0.75) were the closest to zero, indicating limited signal degradation through retinal tissue and the greatest tissue transparency (Fig. 3F). For samples that exhibited poor tissue transparency, the discrepancy between microglial layers was larger, corresponding to slopes of m=-1.4 and m=-1.8 for MACS and Visikol, respectively.

Development of a Hard-setting Clearing Solution (ScaleH) to Enhance Fluorescent Stability in Application Within and Beyond the Retina

Building upon the demonstrated efficacy of ScaleS, we developed a modified clearing formulation, termed ScaleH, by incorporating polyvinyl alcohol (PVA) to produce a hard-setting medium capable of preserving fluorescence signals in cleared tissues. While commercial hard-setting mounting media, such as ProLong Glass antifade mountant, can limit fluorescence signal decay, they are not optimized for mounting cleared tissue. ScaleH was specifically designed to reduce signal decay over time, enabling prolonged visualization in a cleared tissue sample.

Incorporating ScaleH into our optimized immunostaining protocol produced an effective workflow for generating cleared and hardened retinal samples (Fig. 4A). We validated ScaleH by imaging mouse retinas transplanted with human stem cell-derived RGCs. In ScaleH-treated samples, transplanted donor RGCs were clearly visualized within their appropriate retinal layers, providing superior spatial resolution and fluorescence preservation compared to non-cleared samples prepared with ProLong Glass (Fig. 4B).

We subsequently evaluated fluorescence decay in retinal whole mounts between ScaleH and ScaleS4 using the same semi-automated approach described above. Statistical analysis demonstrated a significantly lower fluorescence decay rate for ScaleH (8%) compared to ScaleS4 (40%) over a two-week period (Fig. 4C). Coincubation of samples with DAPI and each clearing solution showed no significant difference between the two formulations, although ScaleH exhibited superior signal retention (Scale S4 DAPI 26% decay, Scale SH DAPI 17% decay).

Lastly, to evaluate the broader applicability of ScaleH, we extended its use to optic nerve tissue (Fig. 4D). En-face imaging of optic nerve samples cleared with ScaleH revealed clear visualization of internal cell nuclei, contrasting with non-cleared ProLong Glass-treated samples that only exhibited superficial nuclei labeling.

Altogether, ScaleH demonstrated robust compatibility with RGC transplantation and optic nerve clearing, showcasing its potential for diverse and novel applications in tissue clearing. These findings also highlight ScaleH's ability to preserve fluorescence signals and facilitate detailed visualization of complex ocular structures.

Discussion

Tissue clearing has been widely adopted across various organ systems, prompting laboratories to optimize protocols based on transparency, ease of use, speed, and fluorescence preservation (Kim et al., 2018). In this study, we systematically evaluated five clearing protocols, ScaleS,

FOCM, OptiMuS, MACS, and Visikol HISTO-1, based on their performance in clearing retinal tissues. Our comparison criteria included tissue transparency, color removal, antibody compatibility, and fluorescence retention. Due to the distinct mechanisms by which clearing agents function and the inherent properties unique to retinal tissues, selecting an optimal clearing protocol is critical.

Among the tested protocols, we identified ScaleS as the most effective clearing solution, showing superior performance across nearly all criteria. To further enhance the utility of ScaleS by limiting fluorophore degradation caused by light exposure, oxygen, or prolonged storage (Piña et al., 2022), we developed a novel clearing solution, ScaleH, by incorporating polyvinyl alcohol into the ScaleS formulation. By combining 15% (w/v) PVA and 15% (w/v) glycerol in deionized water, ScaleH self-hardens around the sample, thus mitigating oxygen infiltration and preserving fluorescence signals for extended periods (Gray & Wess, 1950). Importantly, ScaleH retains the user-friendly nature of ScaleS and does not introduce additional steps or complexity.

In contrast, the two commercial products tested, Visikol HISTO-1 and MACS, had notable limitations. Visikol HISTO-1, an organic solvent-based system, required extensive dehydration steps and introduced tissue fragility and fluorescence degradation despite marginal improvements in transparency over PBS (Villani et al., 2013). Similarly, MACS, an aqueous-based system employing MXDA instead of urea, also required lengthy dehydration steps that reduced fluorescence signals and increased tissue fragility. Neither commercial option proved advantageous over simpler, in-house solutions for routine retinal applications.

Among the other in-house methods, FOCM and OptiMuS, both aqueous-based, sought to simplify the clearing process while minimizing costs. FOCM, which uses DMSO as a polar solvent, achieved substantial tissue transparency but resulted in significant fluorescence loss, limiting its utility for applications involving antibody labeling or fluorescence microscopy. Conversely, OptiMuS provided better fluorescence preservation, albeit with reduced transparency compared to ScaleS, making it a viable secondary choice.

The success of ScaleS can be attributed to its streamlined, two-step approach using ScaleSQ(5) and ScaleS4, along with its excellent fluorescence retention and low cost. These qualities make it particularly well-suited for retinal immunohistochemistry and cell transplantation studies. Our findings underscore its utility in enhancing the visualization and spatial mapping of transplanted RGCs, a critical need in the field given the difficulty of tracking donor cells with limited survival and integration (Oswald et al., 2021)(Ueda et al., 2020)(Zhang et al., 2021)(Soucy et al., 2023a). Previous studies have similarly shown the benefits of tissue clearing to visualize transplanted photoreceptors and axonal mapping, reinforcing the potential broader applicability of ScaleS and the improved ScaleH in retinal regenerative research (Gurdita et al., 2021)(Economo et al., 2019).

Additionally, we demonstrated the broader applicability of ScaleH by successfully clearing optic nerve tissue, suggesting its potential for use across other ocular and neural structures. This whole-tissue clearing capability is particularly impactful for studies involving sparse donor axon projections, such as those expected from transplanted RGCs, where traditional sectioning methods risk missing labeled axons altogether. By enabling intact, three-dimensional imaging of the optic nerve, ScaleH allows comprehensive visualization of donor axon trajectories that would otherwise be under-detected or lost in serial sections.

In conclusion, our development of ScaleH significantly advances tissue-clearing methodologies by combining the simplicity and effectiveness of ScaleS with improved long-term fluorescence stability. Its demonstrated efficacy in both retinal and optic nerve tissues suggests strong promise for broader applications in ocular and neurological research. These capabilities will be critical for future studies in regenerative medicine, offering the structural resolution necessary for evaluating therapeutic interventions in the visual system and beyond.

Figures

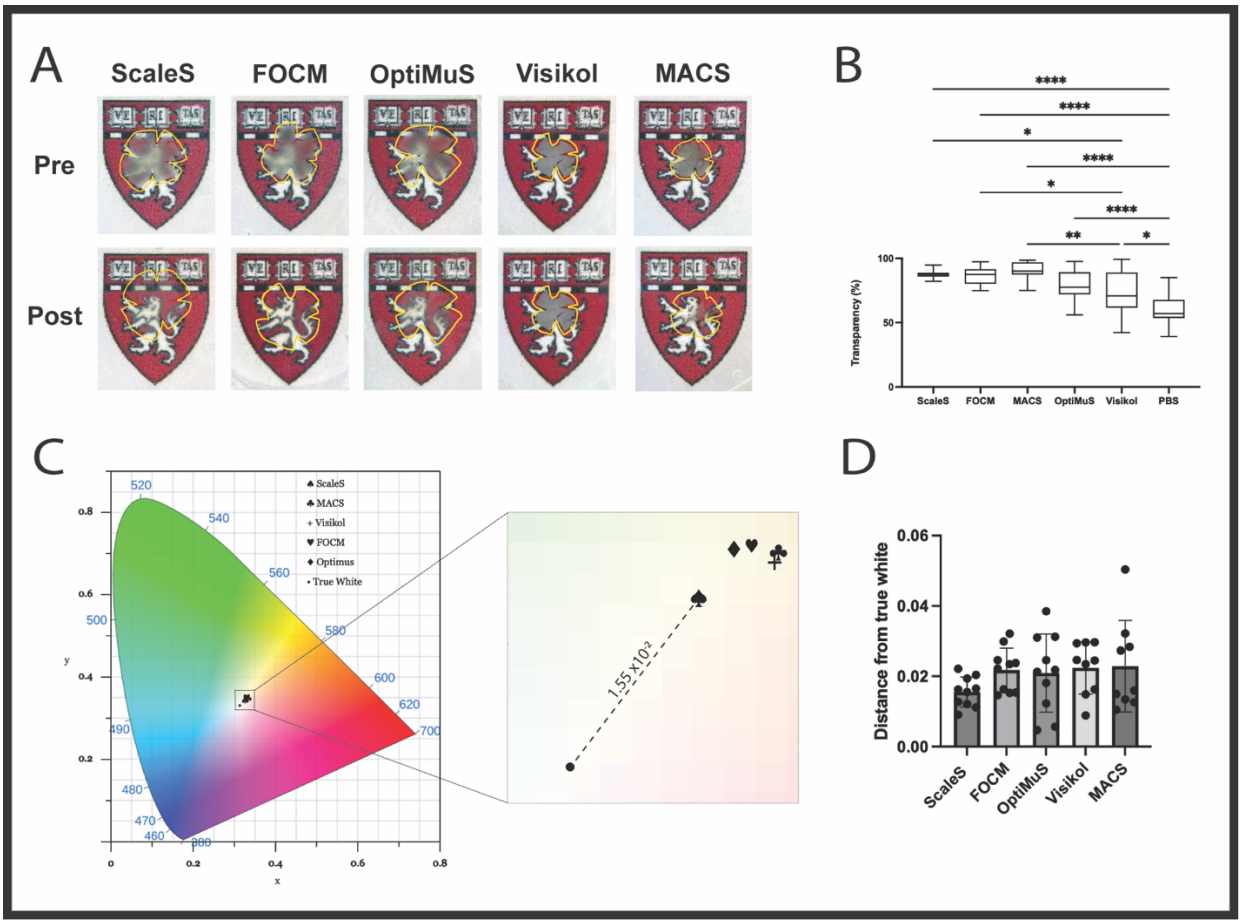

Fig. 1. Visualization of clearing effects on transparency and color of whole-mount retinas. (A) Representative en-face images of ScaleS, FOCM, OptiMuS, Visikol HISTO-1, and MACS samples pre and post-clearing superimposed on the Harvard Medical School logo. **(B)** Quantitative analysis of tissue transparency, defined as the difference between the gray value ratios of the post-clearing and pre-clearing retina-obstructed line and the unobstructed line. N = 10 to 12 retinas per clearing group, 43 retinas for the PBS group. **(C)** CIE 1931 Chromaticity diagram mapping color perception using two CIE parameters, x and y, derived from XYZ and Yxy color spaces. Plotted five clearing agents and true white value with representative distance between ScaleS and true white coordinates. **(D)** Quantitative analysis of the distance between cleared samples and true white, defined as the distance between the average coordinate for true white across all retinas and the average coordinate for each agent. N = 9 to 10 retinas per group.

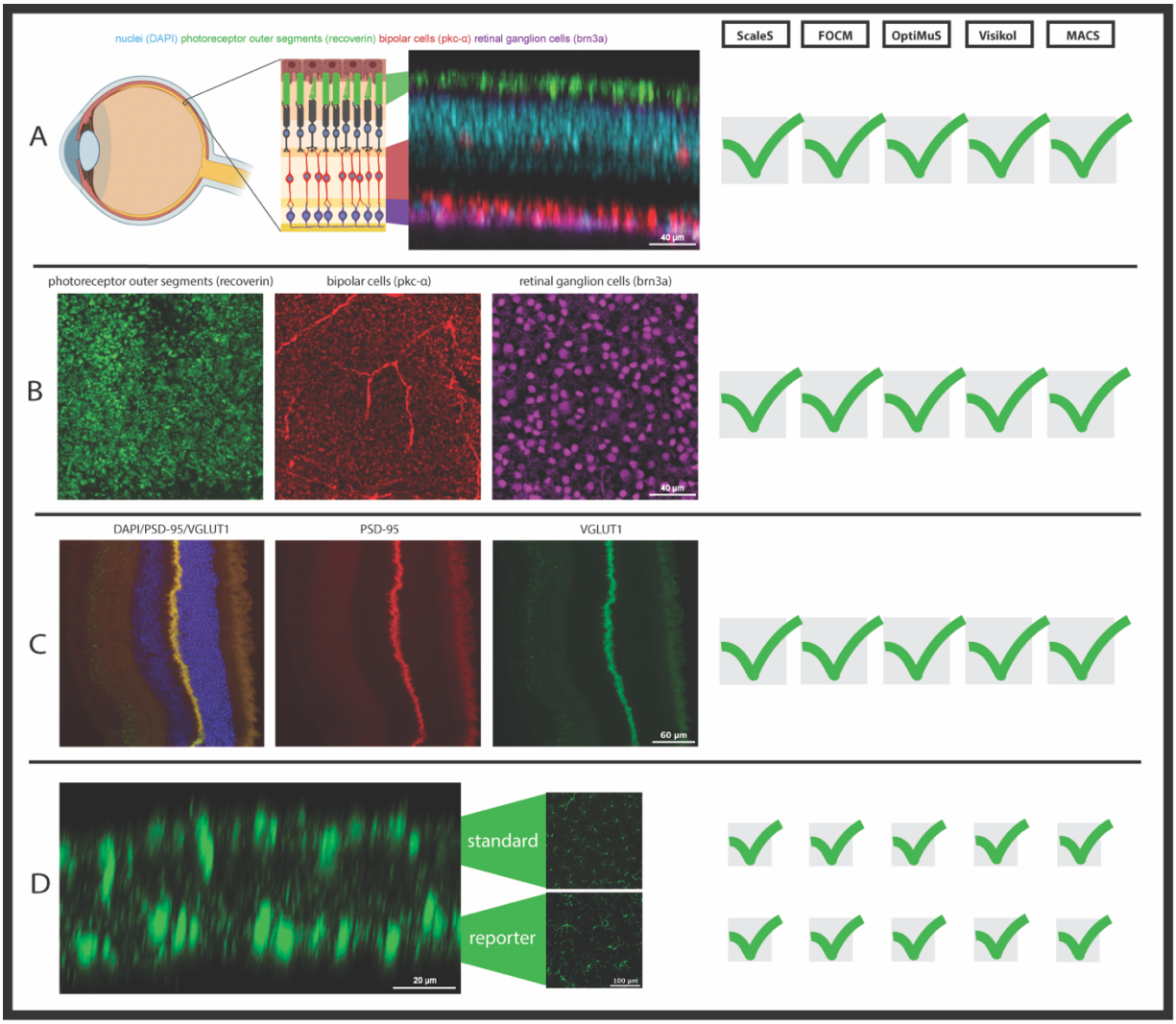

Fig. 2. Observance of macroscopic and microscopic retinal structure immunofluorescence across clearing agents. (A) Representative macroscopic immunofluorescence cross-section of the whole-mount retina with corresponding locations of cells and immunostaining employed

showing clear layering in line with retinal anatomy. **(B)** Representative microscopic immunofluorescence of en-face images of photoreceptor outer segments, bipolar cells, and retinal ganglion cells showing clear visualization of Recoverin, PKC-α, and Brn3a stains. **(C)** Representative en-face images of synaptic microstructures showing the clear visualization of macroscopic DAPI, PSD-95, and VGLUT stain, independent PSD-95 stain, and independent VGLUT stain across clearing agents. **(D)** Representative macroscopic immunofluorescence cross-section of microglia layering within retina showing macrostructural visualization with IBA1. Representative sub-images of en-face IBA1 microglial staining and endogenous reporter microglial staining across clearing agents.

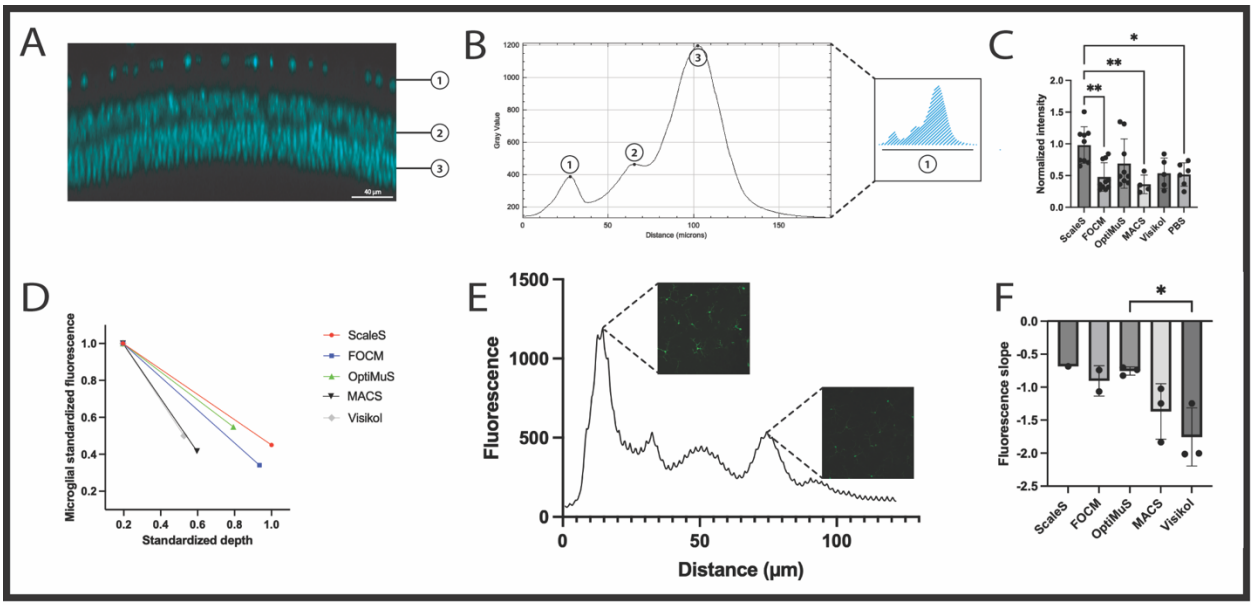

Fig. 3. Clearing agent efficacy across immunohistochemical staining of cell nuclei and microglia. (A) Representative macroscopic immunofluorescence cross-section of whole-mount retina (max intensity projection) stained for DAPI with labeling of (1) retinal ganglion cells, (2) bipolar cells, and (3) photoreceptor outer segments. **(B)** Representative graph of fluorescence intensity with labeled peaks corresponding to each cell layer and schematic of analysis. **(C)** Quantitative analysis of normalized intensity, defined as the average of integrals over the largest first local maximum automated for each cross-section slice output. N = 4 to 10 retinas per group. **(D)** Representative graph of immunohistochemical signal intensity across z position within two microglial layers, with the slope defined as the average of the standardized change in signal intensity between two layers for each clearing solution. **(E)** Representative graph of immunohistochemical signal intensity data across z position within two microglial layers, with greater distance signifying increased depth in the retina. **(F)** Quantitative analysis of the slope between microglial layers for each clearing agent. Each dot represents the slope of a retina. N = 1 to 3 retinas per group.

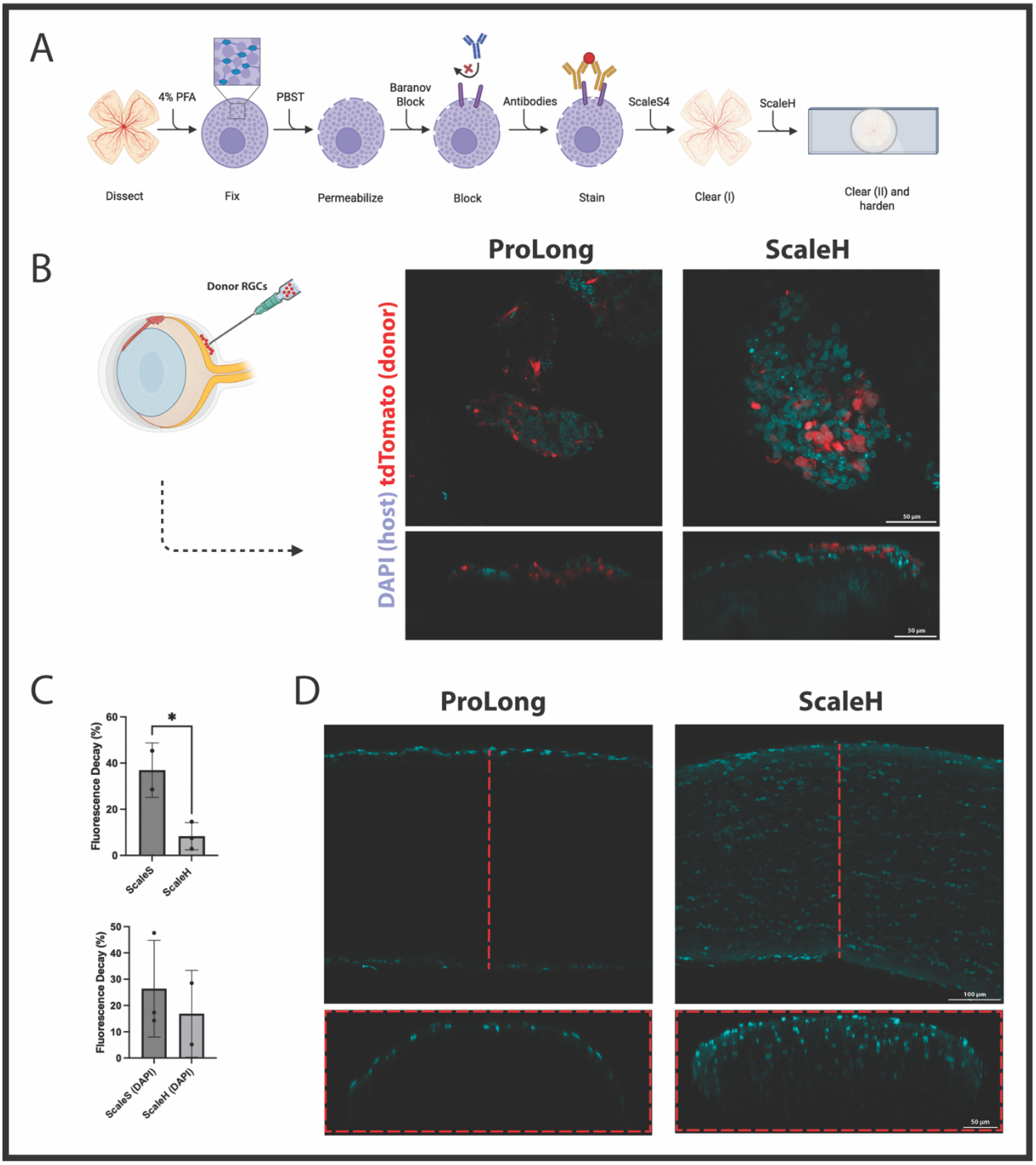

Fig 4. Expanding the use of tissue clearing to novel applications. (A) Schematic overview of mice immunostaining retinal processing with new clearing formulation. **(B)** En-face immunofluorescent images and orthographic projections of human stem cell derived-RGCs (red)

within the subretinal space following transplantation in ProLong Glass (non-cleared) and ScaleH (in-house modified ScaleS solution) samples. **(C)** En-face immunofluorescent images and orthographic projections of cell nuclei in mice optic nerves in ProLong Glass (non-cleared) and ScaleH samples. **(D)** Quantitative analysis of retinal cell nuclei fluorescence decay across unmodified clearing protocol ScaleS and in-house modification ScaleH reveals a significant decrease in signal decay across a two-week period in ScaleH without incubated DAPI. N = 2 to 3 retinas per group.

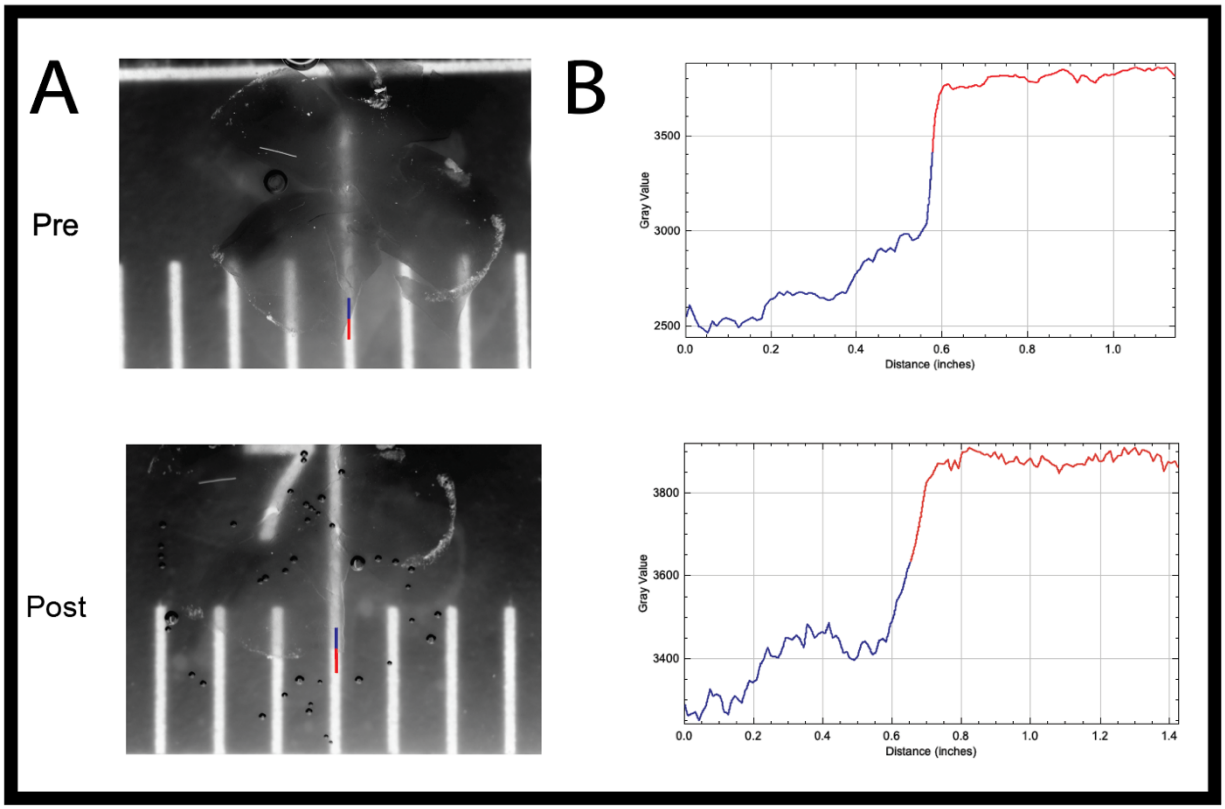

Fig S1. Transparency analysis in pre and post-cleared retina. (A) Representative en-face images of the retina before and after clearing were superimposed on a ruler for analysis. **(B)** Representative ImageJ analysis using the line tool to delineate paths across both unobstructed and retina-obstructed lines and generate an intensity profile plot. Blue demarcation represents obstructed, and red represents unobstructed lines.

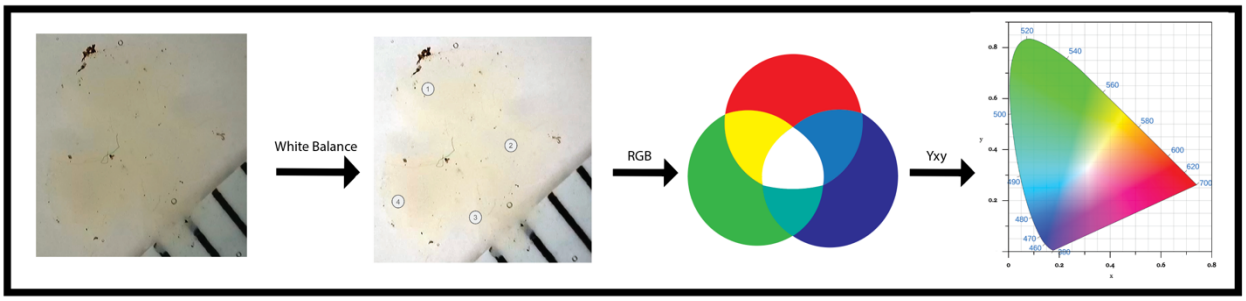

Fig S2. Methodology for color analysis of wholemount retina. Retina images were white-balanced in Adobe Photoshop, and four points on the extremities of the retina were selected. RGB values were measured in Adobe Photoshop and averaged. RGB values were converted to Yxy values using the EasyRGB value converter and plotted on the CIE 1931 chromaticity diagram.

Antigen	Host	Target Cell / Region	Catalog No. / Supplier	Dilution
Recoverin	Rabbit	Photoreceptors	ab5585, Chemicon International	1:500
PKC-α	Mouse	Bipolar cells	sc8393, Santa Cruz Biotechnology	1:500
Brn3a	Guinea pig	Retinal ganglion cells	411 004, Synaptic Systems	1:500
IBA1	Rabbit	Microglia	ab5076, Abcam	1:500
PSD-95	Mouse	Postsynaptic site	N3702-AF647-L, Synaptic Systems	1:300
VGLUT1	Rabbit	Glutamatergic synapses	N1602-At488-L, Synaptic Systems	1:300
mCherry	Chicken	Donor retinal ganglion cells	ab205402, Abcam	1:400

Table S1. Primary antibodies for immunohistochemistry

Bibliography

Cheng, J., McMahon, S. M., Piston, D. W., & Jackson, M. B. (2023). Comparing confocal and two-photon Ca2+ imaging of thin low-scattering preparations. *Biophysical Reports*, *3*(2), 100109. https://doi.org/10.1016/j.bpr.2023.100109

Chung, K., Wallace, J., Kim, S.-Y., Kalyanasundaram, S., Andalman, A. S., Davidson, T. J., Mirzabekov, J. J., Zalocusky, K. A., Mattis, J., Denisin, A. K., Pak, S., Bernstein, H., Ramakrishnan, C., Grosenick, L., Gradinaru, V., & Deisseroth, K. (2013). Structural and molecular interrogation of intact biological systems. *Nature*, *497*(7449), 332–337. https://doi.org/10.1038/nature12107

Economo, M. N., Winnubst, J., Bas, E., Ferreira, T. A., & Chandrashekar, J. (2019). Single-neuron axonal reconstruction: The search for a wiring diagram of the brain. *Journal of Comparative Neurology*, *527*(13), 2190–2199. https://doi.org/10.1002/cne.24674

Ghoraba, H. H., Akhavanrezayat, A., Karaca, I., Yavari, N., Lajevardi, S., Hwang, J., Regenold, J., Matsumiya, W., Pham, B., Zaidi, M., Mobasserian, A., DongChau, A. T., Or, C., Yasar, C., Mishra, K., Do, D., & Nguyen, Q. D. (2022). Ocular Gene Therapy: A Literature Review with Special Focus on Immune and Inflammatory Responses. *Clinical Ophthalmology (Auckland, N.Z.)*, *16*, 1753. https://doi.org/10.2147/OPTH.S364200

Graham, H. K., & Duan, X. (2020). Molecular mechanisms regulating synaptic specificity and retinal circuit formation. *Wiley Interdisciplinary Reviews. Developmental Biology*, *10*(1), e379. https://doi.org/10.1002/wdev.379

Gray, P., & Wess, G. (1950). The Use of Polyvinyl Alcohol and Its Derivatives as Microscopical Mounting Media. Part I.–Water Miscible Mounting Media. *Journal of the Royal Microscopical Society*, *70*(3), 287–291. https://doi.org/10.1111/j.1365-2818.1950.tb04437.x

Gurdita, A., Nickerson, P. E., Pokrajac, N. T., Ortín-Martínez, A., Tsai, E. L. S., Comanita, L., Yan, N. E., Dolati, P., Tachibana, N., Liu, Z. C., Pearson, J. D., Chen, D., Bremner, R., & Wallace, V.

A. (2021). InVision: An optimized tissue clearing approach for three-dimensional imaging and analysis of intact rodent eyes. *iScience*, *24*(8), 102905. https://doi.org/10.1016/j.isci.2021.102905

Hama, H., Hioki, H., Namiki, K., Hoshida, T., Kurokawa, H., Ishidate, F., Kaneko, T., Akagi, T., Saito, T., Saido, T., & Miyawaki, A. (2015). ScaleS: An optical clearing palette for biological imaging. *Nature Neuroscience*, *18*(10), 1518–1529. https://doi.org/10.1038/nn.4107

Hasabeldaim, E. H. H., Swart, H. C., & Kroon, R. E. (2023). Luminescence and stability of Tb doped CaF2 nanoparticles. *RSC Advances*, *13*(8), 5353–5366. https://doi.org/10.1039/D2RA07897J

Hashemi, H., Khabazkhoob ,Mehdi, Nabovati ,Payam, Ostadimoghaddam ,Hadi, Shafaee ,Shokrolah, Doostdar ,Asgar, & and Yekta, A. (2017). The Prevalence of Age-Related Eye Disease in an Elderly Population. *Ophthalmic Epidemiology*, *24*(4), 222–228. https://doi.org/10.1080/09286586.2016.1270335

Hoon, M., Okawa, H., Santina, L. D., & Wong, R. O. (2014). Functional Architecture of the Retina: Development and Disease. *Progress in Retinal and Eye Research*, *42*, 44. https://doi.org/10.1016/j.preteyeres.2014.06.003

Huang, D., Swanson, E. A., Lin, C. P., Schuman, J. S., Stinson, W. G., Chang, W., Hee, M. R., Flotte, T., Gregory, K., Puliafito, C. A., & Fujimoto, J. G. (1991). Optical Coherence Tomography. *Science (New York, N.Y.)*, *254*(5035), 1178. https://doi.org/10.1126/science.1957169

Jagodzinska, J., Sarzi, E., Cavalier, M., Seveno, M., Baecker, V., Hamel, C., Péquignot, M., & Delettre, C. (2017). Optical Coherence Tomography: Imaging Mouse Retinal Ganglion

Cells In Vivo. *Journal of Visualized Experiments : JoVE*, *127*, 55865. https://doi.org/10.3791/55865

Kim, J. H., Jang, M. J., Choi, J., Lee, E., Song, K.-D., Cho, J., Kim, K.-T., Cha, H.-J., & Sun, W. (2018). Optimizing tissue-clearing conditions based on analysis of the critical factors affecting tissue-clearing procedures. *Scientific Reports*, *8*(1), 12815. https://doi.org/10.1038/s41598-018-31153-7

Kim, K., Na, M., Oh, K., Cho, E., Han, S. S., & Chang, S. (2022). Optimized single-step optical clearing solution for 3D volume imaging of biological structures. *Communications Biology*, *5*(1), 1–10. https://doi.org/10.1038/s42003-022-03388-8

London, A., Benhar, I., & Schwartz, M. (2013). The retina as a window to the brain—From eye research to CNS disorders. *Nature Reviews Neurology*, *9*(1), 44–53. https://doi.org/10.1038/nrneurol.2012.227

Matsumoto, K., Mitani, T. T., Horiguchi, S. A., Kaneshiro, J., Murakami, T. C., Mano, T., Fujishima, H., Konno, A., Watanabe, T. M., Hirai, H., & Ueda, H. R. (2019). Advanced CUBIC tissue clearing for whole-organ cell profiling. *Nature Protocols*, *14*(12), 3506–3537. https://doi.org/10.1038/s41596-019-0240-9

Nanegrungsunk, O., Au, A., Sarraf, D., & Sadda, S. R. (n.d.). New frontiers of retinal therapeutic intervention: A critical analysis of novel approaches. *Annals of Medicine*, *54*(1), 1067–1080. https://doi.org/10.1080/07853890.2022.2066169

Oswald, J., Kegeles, E., Minelli, T., Volchkov, P., & Baranov, P. (2021). Transplantation of miPSC/mESC-derived retinal ganglion cells into healthy and glaucomatous retinas.

Molecular Therapy. Methods & Clinical Development, *21*, 180–198. https://doi.org/10.1016/j.omtm.2021.03.004

Piña, R., Santos-Díaz, A. I., Orta-Salazar, E., Aguilar-Vazquez, A. R., Mantellero, C. A., Acosta-Galeana, I., Estrada-Mondragon, A., Prior-Gonzalez, M., Martinez-Cruz, J. I., & Rosas-Arellano, A. (2022). Ten Approaches That Improve Immunostaining: A Review of the Latest Advances for the Optimization of Immunofluorescence. *International Journal of Molecular Sciences*, *23*(3), 1426. https://doi.org/10.3390/ijms23031426

Prahst, C., Ashrafzadeh, P., Mead, T., Figueiredo, A., Chang, K., Richardson, D., Venkaraman, L., Richards, M., Russo, A. M., Harrington, K., Ouarné, M., Pena, A., Chen, D. F., Claesson-Welsh, L., Cho, K.-S., Franco, C. A., & Bentley, K. (2020). Mouse retinal cell behaviour in space and time using light sheet fluorescence microscopy. *eLife*, *9*, e49779. https://doi.org/10.7554/eLife.49779

Ramirez, A. I., Hoz, R. de, Salobrar-Garcia, E., Salazar, J. J., Rojas, B., Ajoy, D., López-Cuenca, I., Rojas, P., Triviño, A., & Ramírez, J. M. (2017). The Role of Microglia in Retinal Neurodegeneration: Alzheimer's Disease, Parkinson, and Glaucoma. *Frontiers in Aging Neuroscience*, *9*, 214. https://doi.org/10.3389/fnagi.2017.00214

Renier, N., Wu, Z., Simon, D. J., Yang, J., Ariel, P., & Tessier-Lavigne, M. (2014). iDISCO: A Simple, Rapid Method to Immunolabel Large Tissue Samples for Volume Imaging. *Cell*, *159*(4), 896–910. https://doi.org/10.1016/j.cell.2014.10.010

Richardson, D. S., & Lichtman, J. W. (2015). Clarifying Tissue Clearing. *Cell*, *162*(2), 246–257. https://doi.org/10.1016/j.cell.2015.06.067

Sluch, V. M., Chamling, X., Liu, M. M., Berlinicke, C. A., Cheng, J., Mitchell, K. L., Welsbie, D. S., & Zack, D. J. (2017). Enhanced Stem Cell Differentiation and Immunopurification of Genome Engineered Human Retinal Ganglion Cells. *Stem Cells Translational Medicine*, *6*(11), 1972–1986. https://doi.org/10.1002/sctm.17-0059

Soucy, J. R., Aguzzi, E. A., Cho, J., Gilhooley, M. J., Keuthan, C., Luo, Z., Monavarfeshani, A., Saleem, M. A., Wang, X.-W., Wohlschlegel, J., Fouda, A. Y., Ashok, A., Moshiri, A., Chedotal, A., Reed, A. A., Askary, A., Su, A.-J. A., La Torre, A., Jalligampala, A., … The RReSTORe Consortium. (2023a). Retinal ganglion cell repopulation for vision restoration in optic neuropathy: A roadmap from the RReSTORe Consortium. *Molecular Neurodegeneration*, *18*(1), 64. https://doi.org/10.1186/s13024-023-00655-y

Soucy, J. R., Todd, L., Kriukov, E., Phay, M., Malechka, V. V., Rivera, J. D., Reh, T. A., & Baranov, P. (2023b). Controlling donor and newborn neuron migration and maturation in the eye through microenvironment engineering. *Proceedings of the National Academy of Sciences*, *120*(46), e2302089120. https://doi.org/10.1073/pnas.2302089120

Tomer, R., Ye, L., Hsueh, B., & Deisseroth, K. (2014). Advanced CLARITY for rapid and high-resolution imaging of intact tissues. *Nature Protocols*, *9*(7), 1682–1697. https://doi.org/10.1038/nprot.2014.123

Ueda, H. R., Ertürk, A., Chung, K., Gradinaru, V., Chédotal, A., Tomancak, P., & Keller, P. J. (2020). Tissue clearing and its applications in neuroscience. *Nature Reviews. Neuroscience*, *21*(2), 61–79. https://doi.org/10.1038/s41583-019-0250-1

Villani, T. S., Koroch, A. R., & Simon, J. E. (2013). An improved clearing and mounting solution to replace chloral hydrate in microscopic applications. *Applications in Plant Sciences*, *1*(5), 1300016. https://doi.org/10.3732/apps.1300016

Zhang, K. Y., Aguzzi, E. A., & Johnson, T. V. (2021). Retinal Ganglion Cell Transplantation: Approaches for Overcoming Challenges to Functional Integration. *Cells*, *10*(6), 1426. https://doi.org/10.3390/cells10061426

Zhu, J., Ma, Y., Xu, J., Li, Y., Wan, P., Qi, Y., Yu, T., & Zhu, D. (2021). Dec-DISCO: Decolorization DISCO clearing for seeing through the biological architectures of heme-rich organs. *Biomedical Optics Express*, *12*(9), 5499–5513. https://doi.org/10.1364/BOE.431397

Zhu, J., Yu, T., Li, Y., Xu, J., Qi, Y., Yao, Y., Ma, Y., Wan, P., Chen, Z., Li, X., Gong, H., Luo, Q., & Zhu, D. (2020). MACS: Rapid Aqueous Clearing System for 3D Mapping of Intact Organs. *Advanced Science*, *7*(8), 1903185. https://doi.org/10.1002/advs.201903185

Zhu, X., Huang, L., Zheng, Y., Song, Y., Xu, Q., Wang, J., Si, K., Duan, S., & Gong, W. (2019). Ultrafast optical clearing method for three-dimensional imaging with cellular resolution. *Proceedings of the National Academy of Sciences*, *116*(23), 11480–11489. https://doi.org/10.1073/pnas.1819583116

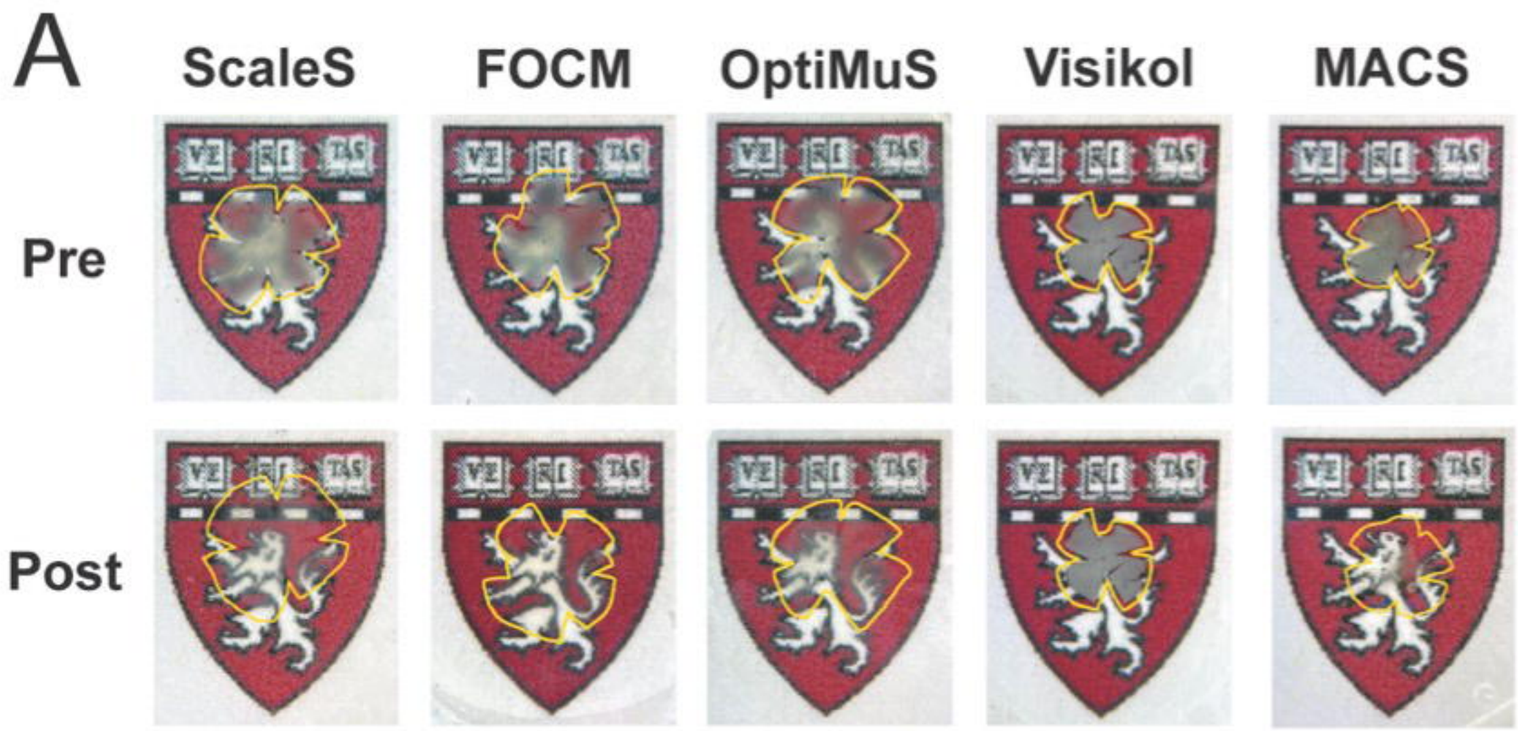
A
ScaleS
FOCM
OptiMuS
Visikol
MACS
Pre
Post

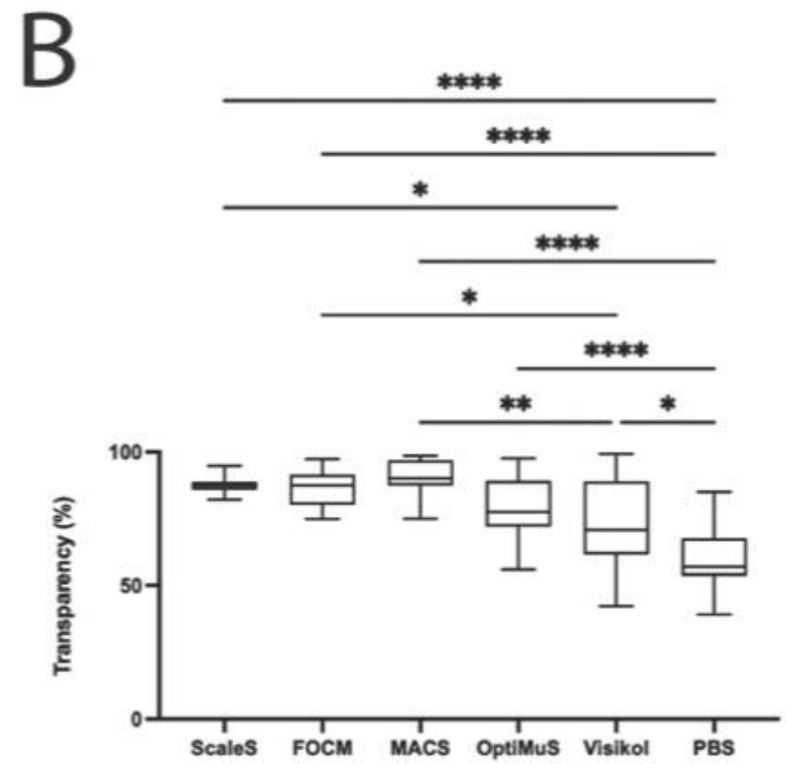
B
****
****
*
****
*
****
**
*
100
50
0
Transparency (%)
ScaleS
FOCM
MACS
OptiMuS
Visikol
PBS

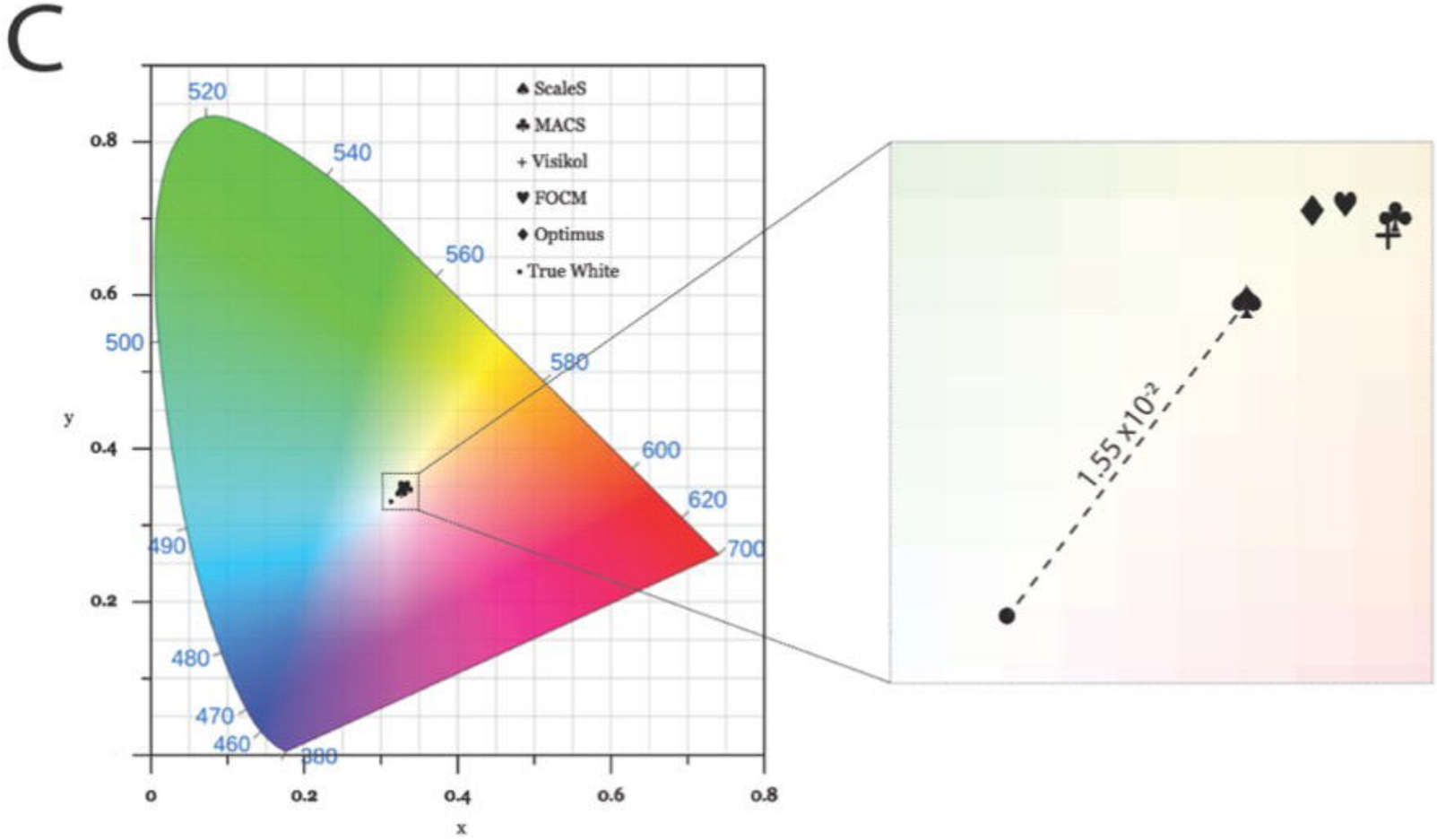
C
ScaleS
MACS
Visikol
FOCM
Optimus
True White
520
540
560
580
600
620
700
500
490
480
470
460
0.8
0.6
0.4
0.2
y
0
0.2
0.4
0.6
0.8
x
1.55 x10-2

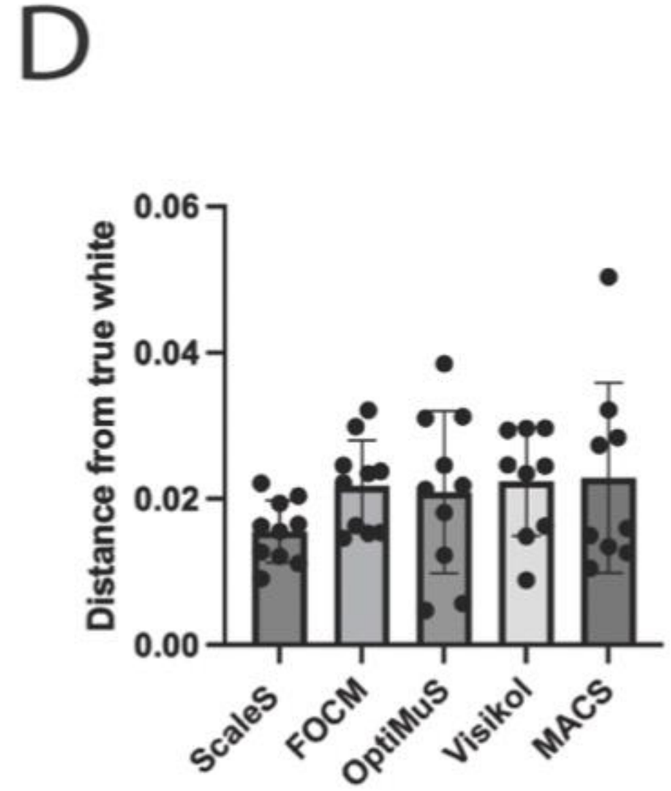
D
0.06
0.04
0.02
0.00
Distance from true white
ScaleS
FOCM
OptiMuS
Visikol
MACS

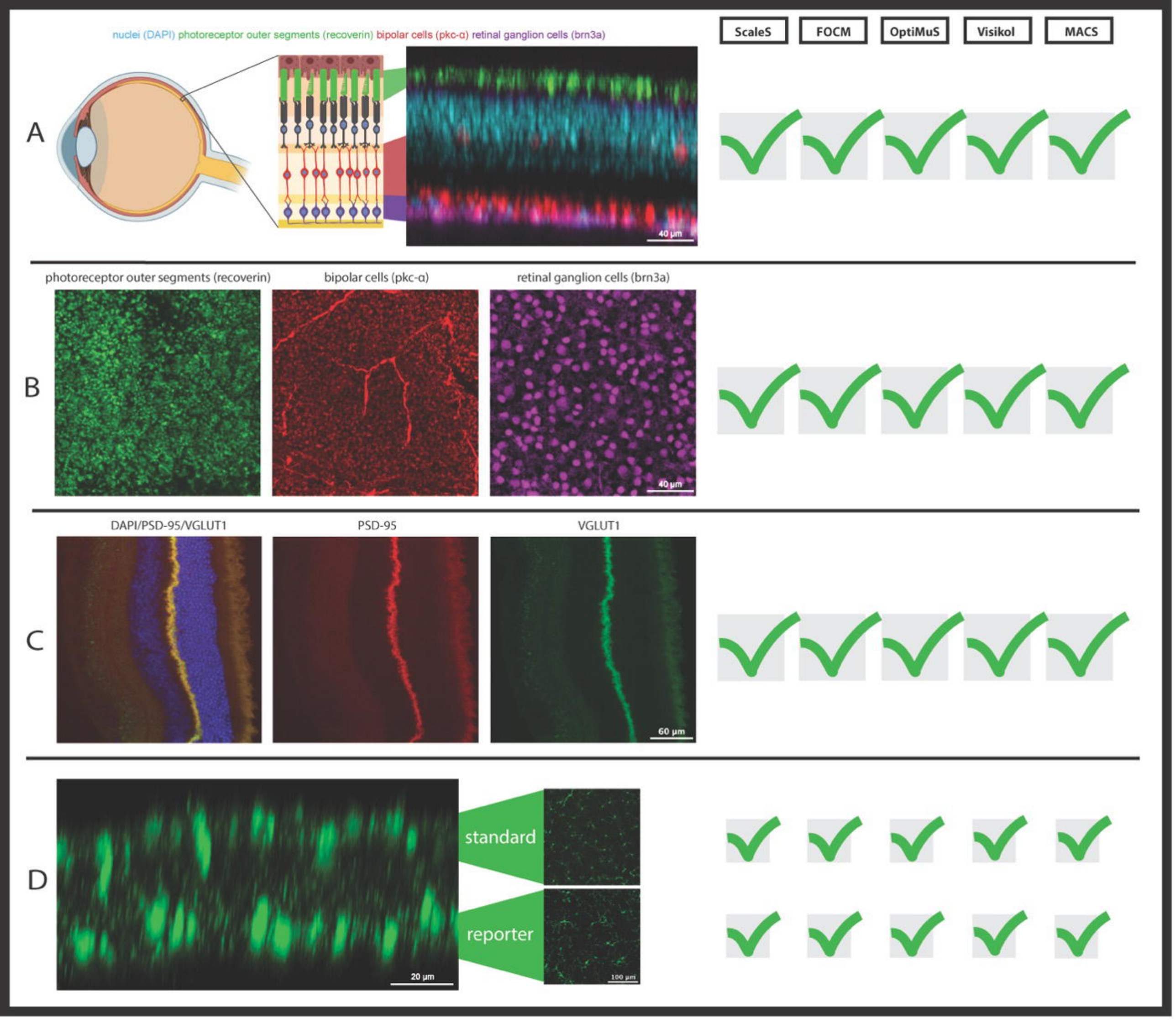
ScaleS
FOCM
OptiMuS
Visikol
MACS
A
nuclei (DAPI) photoreceptor outer segments (recoverin) bipolar cells (pkc-α) retinal ganglion cells (brn3a)
40 µm
B
photoreceptor outer segments (recoverin)
bipolar cells (pkc-α)
retinal ganglion cells (brn3a)
40 µm
C
DAPI/PSD-95/VGLUT1
PSD-95
VGLUT1
60 µm
D
standard
reporter
20 µm
100 µm

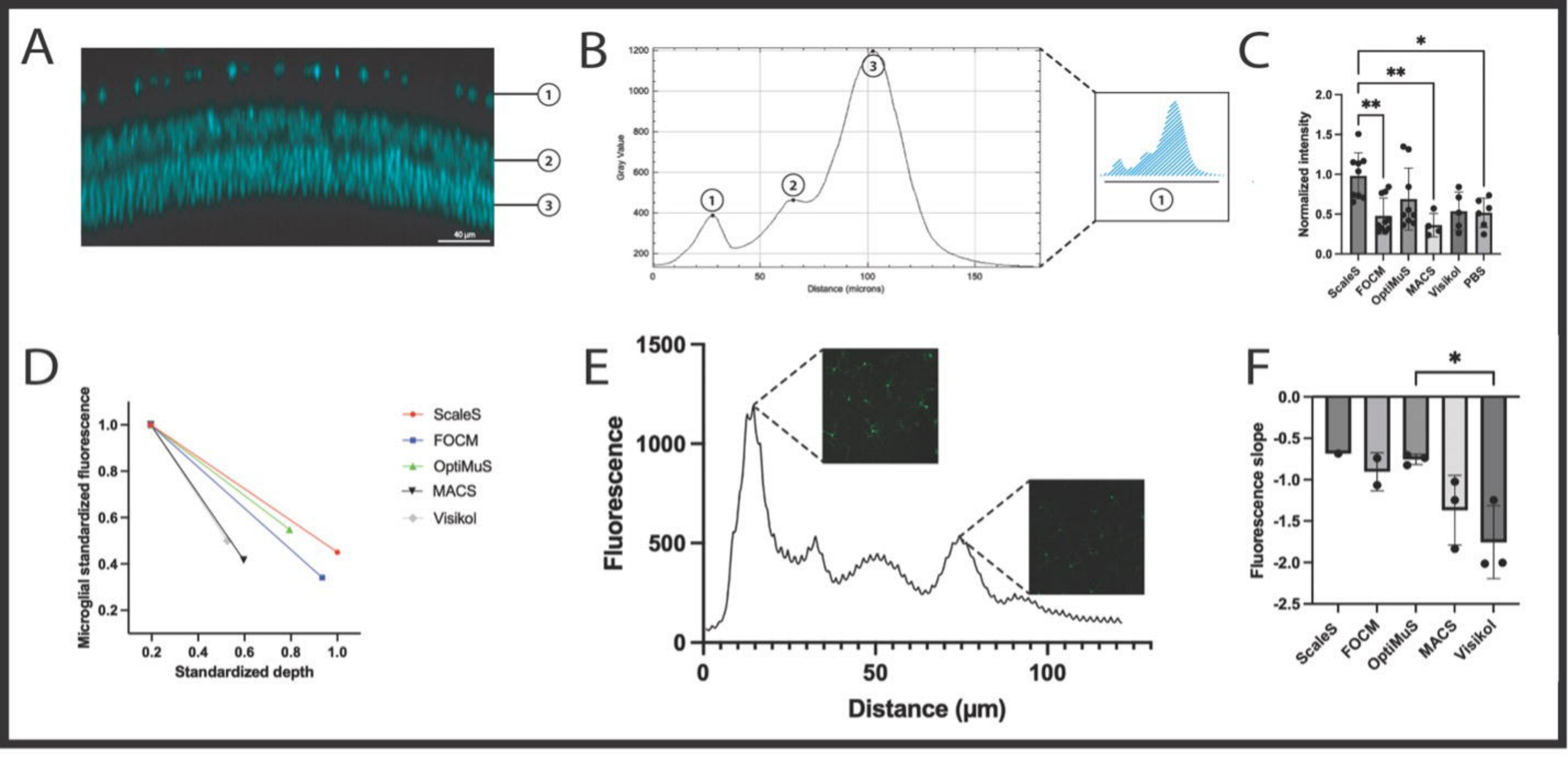
A
1
2
3
40 µm
B
Gray Value
Distance (microns)
C
Normalized intensity
ScaleS
FOCM
OptiMuS
MACS
Visikol
PBS
D
Microglial standardized fluorescence
Standardized depth
ScaleS
FOCM
OptiMuS
MACS
Visikol
E
Fluorescence
Distance (µm)
F
Fluorescence slope
ScaleS
FOCM
OptiMuS
MACS
Visikol

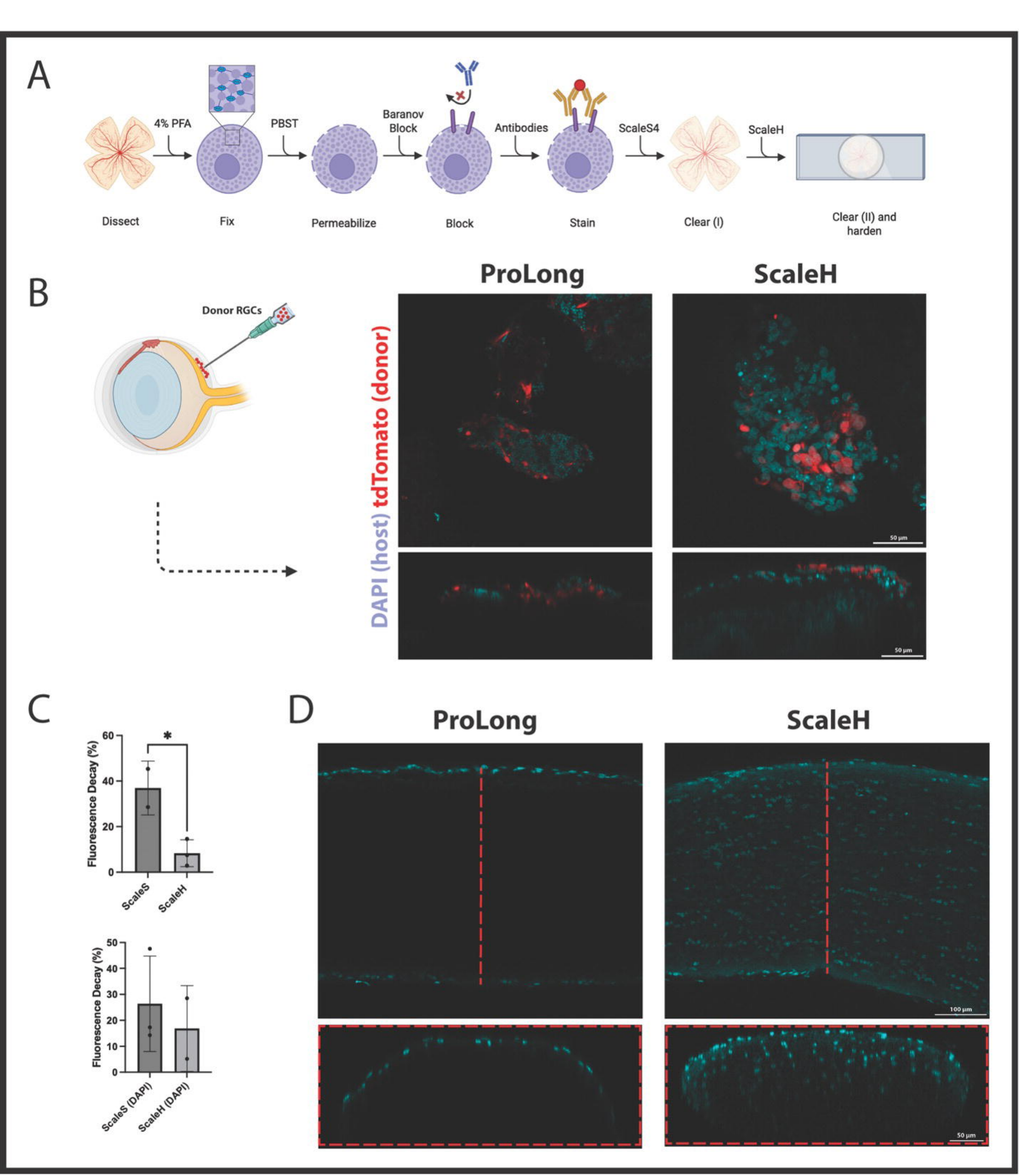
A
4% PFA
PBST
Baranov Block
Antibodies
ScaleS4
ScaleH
Dissect
Fix
Permeabilize
Block
Stain
Clear (I)
Clear (II) and harden
B
Donor RGCs
ProLong
ScaleH
DAPI (host) tdTomato (donor)
50 µm
50 µm
C
Fluorescence Decay (%)
60
40
20
0
*
ScaleS
ScaleH
Fluorescence Decay (%)
50
40
30
20
10
0
ScaleS (DAPI)
ScaleH (DAPI)
D
ProLong
ScaleH
100 µm
50 µm

A

Pre

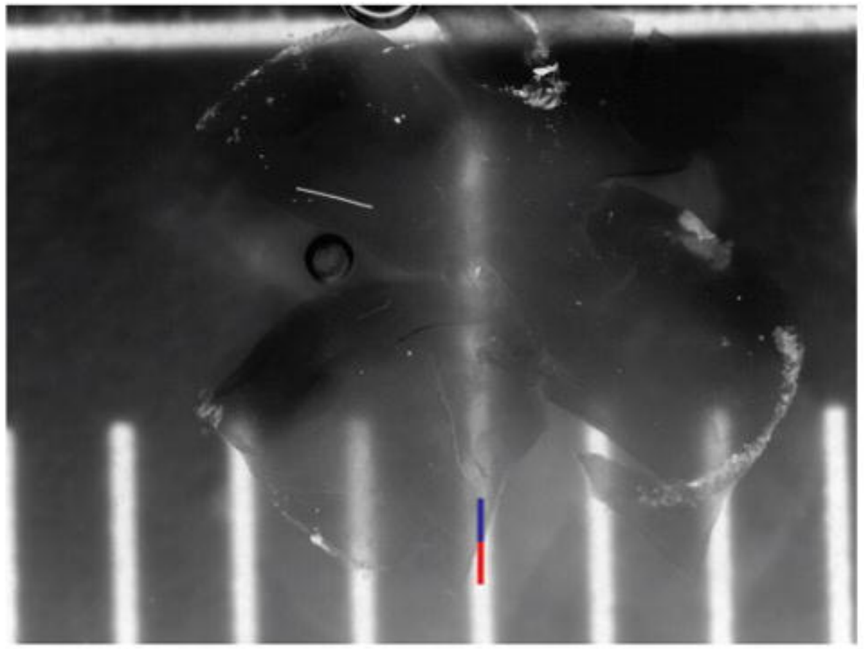

B

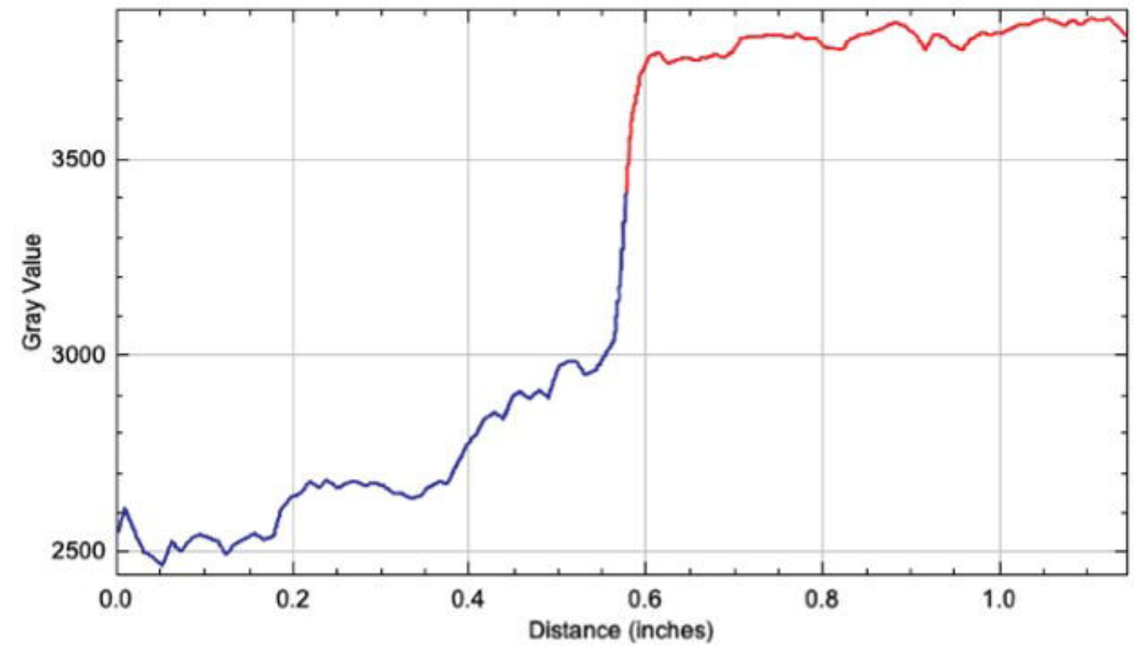
Gray Value
3500
3000
2500
0.0
0.2
0.4
0.6
0.8
1.0
Distance (inches)

Post

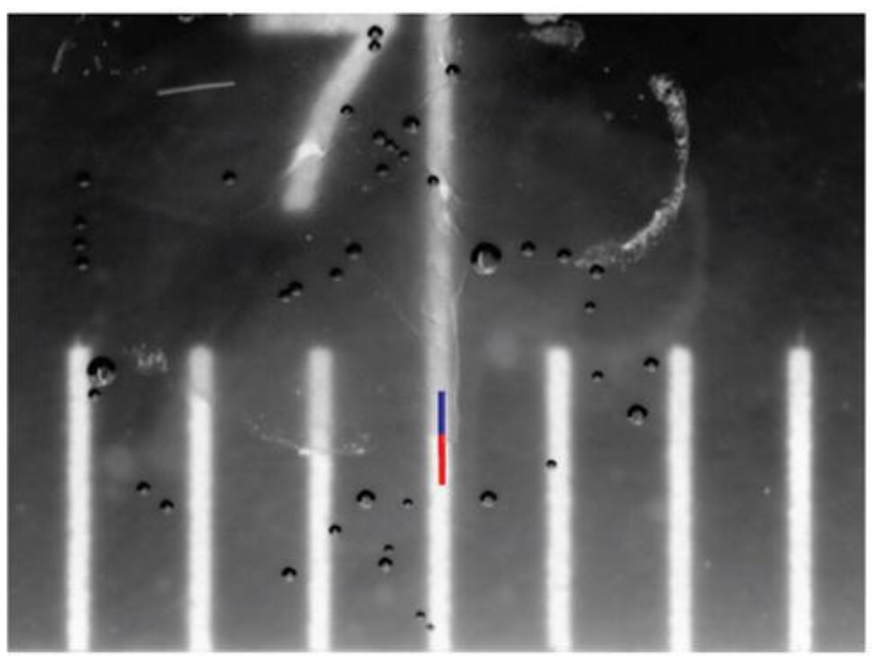

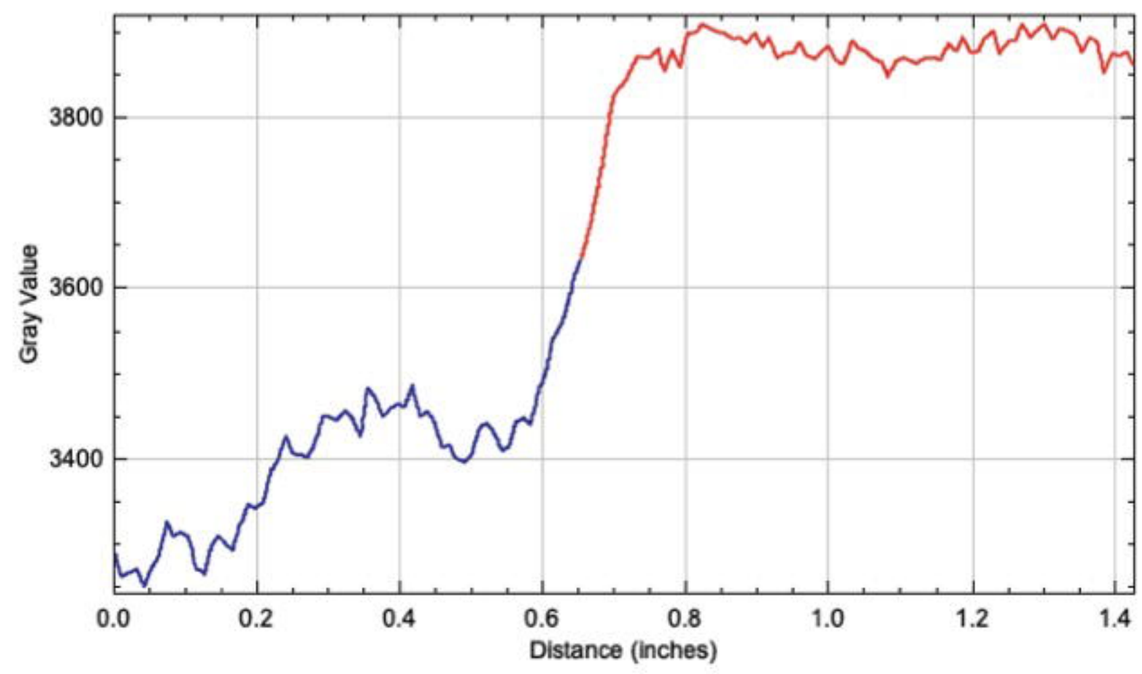
Gray Value
3800
3600
3400
0.0
0.2
0.4
0.6
0.8
1.0
1.2
1.4
Distance (inches)

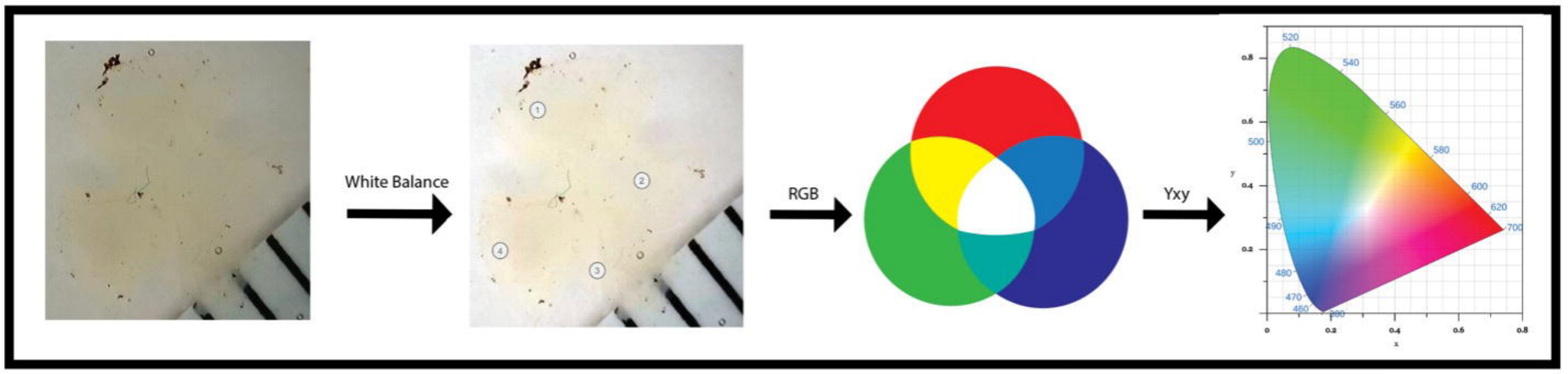
White Balance
1
2
3
4
RGB
Yxy
520
540
560
580
600
620
700
500
490
480
470
460
0.8
0.6
0.4
0.2
0
0.2
0.4
0.6
0.8
x
y